Heliyon 10 (2024) e40553

Contents lists available at ScienceDirect

Heliyon

journal homepage: www.cell.com/heliyon

Research article

Enhanced irradiation-resistance in NbMoTaW refractory high-entropy alloy via rhenium addition

Li Huang [a,*], Shuo Sun [a], Jianrong Xue [a], Xiaohui Lin [a], Xuanqiao Gao [a], Yanchao Li [a], Jianfeng Li [a], Chunfang Ma [b,**], Wen Zhang [a]

[a] *Northwest Institute for Nonferrous Metal Research, Xi'an, 710016, China*
[b] *School of Materials Science and Engineering, Xi'an Polytechnic University, China*

ARTICLE INFO

Keywords:
Refractory high-entropy alloys (RHEAs)
Radiation damage
Defects
Deformation and fracture
NbMoTaWRe

ABSTRACT

The He^{2+} irradiation-induced mechanical and microstructural evolutions were studied in $Nb_{25}Mo_{25}Ta_{25}W_{25}$ (at.%) and $Nb_{20}Mo_{20}Ta_{20}W_{20}Re_{20}$ (at.%) refractory high-entropy alloys (RHEAs) films, respectively. The addition of Re reduces the yield stress, while improves the ductility in as-deposited NbMoTaW RHEA film. After He^{2+} irradiation at room temperature, grain boundary brittleness is much severe in NbMoTaW RHEA film than in NbMoTaWRe RHEA film. The addition of Re enhances lattice distortion, leading amorphous regions with several nanometers forms in the grain boundaries in NbMoTaWRe RHEA film. In additionn, grain sizes in NbMoTaWRe RHEA are much smaller than in NbMoTaW RHEA. Excess volumes facilitate the annihilation of damages caused by He ions bombardment. He bubbles mainly distributes along grain boundaries in NbMoTaW RHEA film. The bubble size decreases and becomes hard to discern in NbMoTaWRe RHEA film. Thus, hardening effect induced by He irradiation is less obvious in NbMoTaWRe than in NbMoTaW RHEA film. In summary, the addition of Re to NbMoTaW RHEA effectively improves irradiation-resistance.

1. Introduction

High-entropy alloys (HEAs) with FCC structures have excellent properties, such as mechanical and irradiated properties at room temperature [1–3] What is more, porous high-entropy alloys are acted as efficient electrocatalysts that has a potential application [4–6]. While, strength drops obviously in FCC HEAs at high temperature (>800 °C) [7]. To explore HEAs with stable properties at high temperature, many researchers have focused on refractory high-entropy alloys (RHEAs) that are composed mainly by refractory alloys [8,9]. Xiong et al. explore the response of WTaTi, WTaCrV, and WTaCrVTi under He implantation and compare the results with pure W, which proposes higher irradiation resistance in RHEAs than in W [10]. Radiation-induced amorphization of RHEA is reported and the finding challenges the current understanding of phase stability of RHEAs upon irradiation [11]. In Li's research, self-healing behavior are observed in TiTaNbZr films that was revealed on account of the enhanced diffusion and redistribution of atoms, which could also lead to a decrease of irradiation defects [12]. What is more, functional W composites are successfully justified as potential applications in radiation shielding field [13–17].

* Corresponding author.
** Corresponding author.
E-mail addresses: huangli46272@163.com (L. Huang), mx_mcf@163.com (C. Ma).

https://doi.org/10.1016/j.heliyon.2024.e40553
Received 17 March 2024; Received in revised form 10 November 2024; Accepted 18 November 2024
Available online 19 November 2024

NbZrTi-based HREAs are widely well studied [18–22], for example, Pu et al. reveal that irradiation-enhanced surface blisters in TaTiNbZr RHEA were strongly dependent on He plasma energy [18]. In Chang' results, the swelling and hardening effects in HfNbTaTiZr RHEA were significantly suppressed compared to those of conventional nuclear materials [19]. According to the structural stability under high temperature irradiation, significant irradiation-enhanced precipitation with Hf and Zr enrichment is observed in HfNbZrTi RHEA [20].

To improve stability at high temperature, Senkov et al. successfully prepared equal atomic ratio NbMoTaW and NbMoTaWV refractory high-entropy alloys (RHEAs) with single-phase BCC structure in 2010 [21]. These RHEAs possess excellent mechanical properties at high temperature (1600 °C) [22]. In addition, Ren et al. assumed high irradiation-resistance in NbMoTaW RHEA by first - principle calculations [23]. However, the ductility of NbMoTaW RHEA at room temperature is pretty bad, which is similar to tungsten alloys and molybdenum alloys [24]. Lots of researches have shown that the addition of rhenium (Re) can effectively reduce the ductile-brittle transition temperature of W and Mo, and improve the room temperature strength, elongation and irradiated properties, which is also called as "rhenium effect" [25].

The "rhenium effect" methods have been successfully applied to NbMoTaW RHEAs [26,27]. For example, Zhang et al. justified that ductility at room temperature increases from 2.6 % in NbMoTaW to 7.0 % in $NbMoTaWRe_{0.5}$ [27]. Zhang et al. verified the addition of Re did not affect the single-phase BCC structure in multi-elements RHEAs [28]. In addition, the addition of Re is also beneficial to irradiation-resistance in Mo alloys [29] and W alloys [30], which may make NbMoTaW RHEA excellent mechanical and irradiation properties. Therefore, the effects of Re on the mechanical and irradiated responses in NbMoTaW RHEA are discussed in this work.

2. Materials and methods

Magnetron sputtering was used to prepared $Nb_{25}Mo_{25}Ta_{25}W_{25}$ (at.%) and $Nb_{20}Mo_{20}Ta_{20}W_{20}Re_{20}$ (at.%) refractory high-entropy alloys (RHEAs) films, on Si (111) substrate at room temperature (RT). The targets are alloyed $Nb_{25}Mo_{25}Ta_{25}W_{25}$ (at.%) and $Nb_{20}Mo_{20}Ta_{20}W_{20}Re_{20}$, respectively, to ensure the composed elements distribute uniformly. Sputtering begins as vacuum pressure reaches to 6.0×10^{-4} Pa. Ar pressure maintains at $\sim 5.0 \times 10^{-1}$ Pa during sputtering. The deposition duration is 2 h, and the total film thicknesses of NbMoTaW and NbMoTaWRe are 3.3 μm and 2.3 μm, respectively.

He ion implantation experiments were performed at RT with ion energy of 120 keV, to facilitate the fabrication of samples for tests. The total fluences is 1×10^{16} ions/cm^2 with dose rate 1×10^{13} ions/cm^2/s. The duration of irradiation exposure is 1000 s. The displacement per atom (dpa) values and He concentration were calculated by stopping and range of ions in matter (SRIM-2013) software with a threshold energy for 60 eV [31] in "full Damage F-C mode".

The phase structures were detected by via X-ray diffraction (XRD) with Cu target and field emission transmission electron microscopy (FEI Talos F200×). The distribution of composed elements is detected by energy dispersive spectrometer (EDS) operating at TEM. Hardness values before and after irradiation were tested via nanoindentation test (MTS Nanoindenter XP) with maximum depths

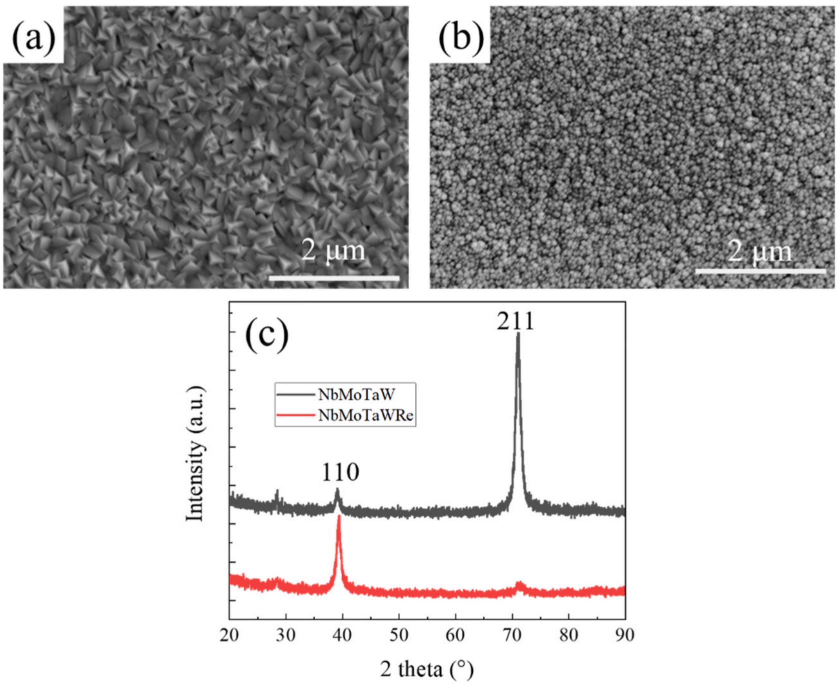

Fig. 1. Microstructural features of NbMoTaW and NbMoTaWRe RHEAs before irradiation. (a) and (b) are the surface features (SEM) for NbMoTaW and NbMoTaWRe RHEAs, respectively. XRD patterns are shown in (c).

of 200 nm. For each sample, 10 indents were carried out to ensure the results. Strain rate was set at 0.05 s^{-1} under continuous stiffness measurement (CSM) mode. The cross-sectional samples and micro-pillars were prepared by FEI Helios (NanoLab 600i) FIB/SEM dual focused-ion-beam (FIB) system. The diameter of pillars was set as ~1.7 μm with height-diameter ratio 2:1. In-situ SEM micro-pillar compression (PI88) tests were conducted at RT with loading rate 1 nm/s. At least two data were tested for each sample.

3. Results and discussions

As are shown in Fig. 1(a) and (b), surface features of NbMoTaW and NbMoTaWRe RHEAs are distinguished before irradiation. Lots of triangle-like boundaries are visible on NbMoTaW RHEA surface. While, round cluster boundaries appear on NbMoTaWRe RHEA surface, meaning different growing rates between NbMoTaW and NbMoTaWRe RHEAs [32]. XRD patterns that shown in Fig. 1(c) justify both NbMoTaW and NbMoTaWRe RHEAs have single BCC phase. The peaks in Fig. 1(c) are marked as [110] and [211], respectively.

Fig. 2(a) and (b) are high-angle annular dark field images of NbMoTaW and NbMoTaWRe RHEAs. Obvious columnar crystals form during sputtering. In addition, the addition of Re effectively refines grain size NbMoTaW RHEA. Generally, the EDS results in (a-I)-(a-IV) and (b-I)-(b-V) represent the uniform distributions of constituent elements in both NbMoTaW and NbMoTaWRe RHEAs. However, Ta content rises from 25 at.% in the middle part of film to ~30 at.% in the region near surface, which may induced by the local Ta segregation in NbMoTaW target. What is more, the insert in Fig. 2(a) is the corresponding line scanning EDS result, which also justifies the uniform distributions of Nb, Mo, Ta and W.

The SRIM results for NbMoTaW and NbMoTaWRe RHEAs are shown in Fig. 3(a) and (b), respectively. Both He distribution and irradiated damage distribute in regions with width 400 nm. Fig. 3(c) compares the He distributions between NbMoTaW and NbMoTaWRe RHEAs, in which the peak value in NbMoTaWRe is a bit smaller than in NbMoTaW.

Microstructural features of NbMoTaW and NbMoTaWRe RHEAs detected by TEM are shown in Fig. 4(a) and (b), respectively. Grain size in NbMoTaW RHEA is much larger than in NbMoTaWRe RHEA. In addition, amorphous bands with width several nanometers form in grain boundaries, as marked as bule square in Fig. 4(b) that shows the FFT (Fast Fourier Transfer) result for region B. The lattice distortion in NbMoTaWRe RHEA is much higher than in NbMoTaW RHEA in inner grain, as marked in yellow square in Fig. 4(a) and the green square in Fig. 4(b). The corresponding FFT-filtered - IFFT images for region A and C are shown in Fig. 4(a-II) and 4(b-II). Therefore, the number of excess volumes increases in NbMoTaW RHEA after adding Re. The excess volumes supply more sites for irradiation-induced damages to annihilate in NbMoTaWRe RHEA.

Fig. 5(a) and (b) shows representative load - displacement curves of NbMoTaW and NbMoTaWRe RHEAs before and after irradiation under nano-indentation tests. The load values for irradiated NbMoTaW RHEA are little higher than un-irradiated one under the same displacement. However, no obvious hardening induced by RT irradiation in NbMoTaWRe RHEA. Compressive strength in irradiated one decreases in NbMoTaW RHEA, while enhances in NbMoTaWRe RHEA, as shown in Fig. 5(c). It is noted that the compressive strains in NbMoTaWRe RHEA reach to ~0.065 and 0.055 in the un-irradiated and irradiated ones, respectively, before compressive stresses drop remarkably. The embrittlement in grain boundaries of irradiated NbMoTaW RHEA is much more severe than un-irradiated one, as shown in Fig. 5(d). Thus, both the results of nano-indentation tests and micro-pillar compressions verify that NbMoTaWRe RHEA possesses better irradiation-resistance than NbMoTaW RHEA.

In previous researches, Guo et al. have studied irradiated response of nanocrystalline NbMoTaW and NbMoTaWV HEAs films after helium ions irradiation [33]. NbMoTaWV RHEA films were discovered to produce smaller helium bubbles and less pronounced microcracks compared to NbMoTaW RMPEA films. It was due to the solid solution incorporation of V which further enhanced the

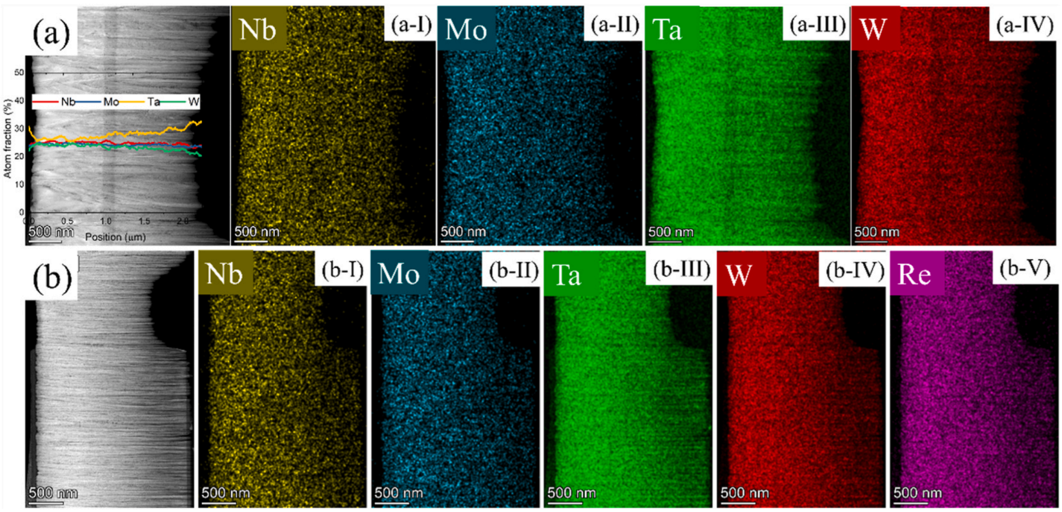

Fig. 2. EDS results for NbMoTaW in (a) and NbMoTaWRe RHEAs in (b), respectively, the insert in (a) is the corresponding line scanning EDS result.

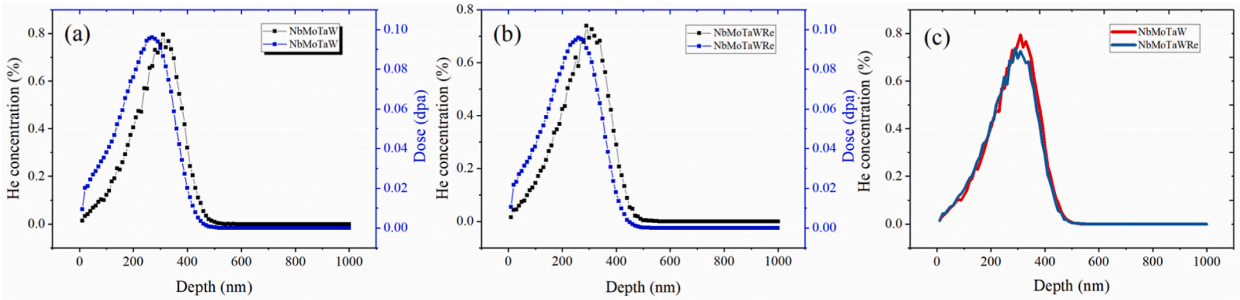

Fig. 3. SRIM results for NbMoTaW in (a) and NbMoTaWRe RHEAs in (b), respectively, the differences of He concentration are shown in (c).

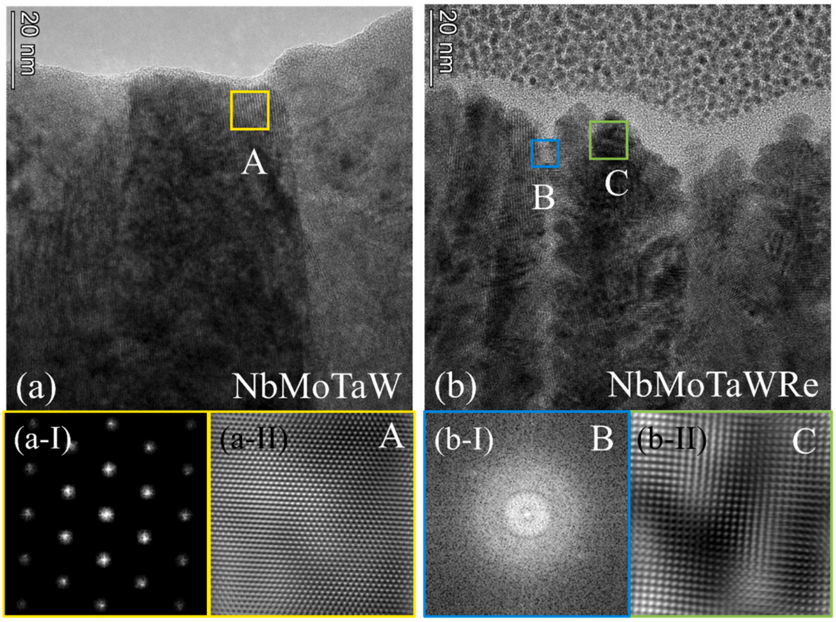

Fig. 4. Microstructural features of NbMoTaW and NbMoTaWRe RHEAs detected by TEM in (a) and (b), respectively, with (a-I) and (a-II) are corresponding FFT and IFFT images for region A in (a), with (b-I) and (b-II) are corresponding FFT and IFFT images for regions B and C in (b).

lattice distortion and toughness as well as the profound suppression of helium diffusion. The results in our work justify the similar effect of V and Re to NbMoTaW RHEA film. In addition, the mechanical responses after irradiation have also been evaluated in this work, i.e. He bubbles in NbMoTaW RHEA film severely accelerate the brittlement of grain boundary.

Fig. 6(a–I) and 6(b-I) show TEM patterns for NbMoTaW and NbMoTaWRe RHEAs after irradiation, respectively. The inserts in Fig. 6(a–I) and 6(b-I) are the corresponding He concentration. To observe He bubble, TEM images with under-focus (−500 nm) are given in Fig. 6(a-II) and 6(b-II), with over-focus (+500 nm) are given in Fig. 6(a-III) and 6(b-III). He bubbles segregate and line up in grain boundaries irradiated NbMoTaW RHEA in the damage region, as marked as the yellow ellipses in Fig. 6(a-II) and 6(a-III). He bubbles are larger in grain boundaries than in inner NbMoTaW RHEA, attributing to severe embrittlement in grain boundaries. However, no obvious He bubbles are observed in NbMoTaWRe RHEA, suggesting He bubbles are smaller in NbMoTaWRe RHEA than in NbMoTaW RHEA. In addition, the segregations of He bubbles to grain boundaries are also invisible in NbMoTaWRe. Therefore, irradiation-resistance is effectively enhanced in NbMoTaW RHEA via adding Re.

When lots of He^{2+} ions with high energy knock n metal materials, structural changes occur. For example, the number of interstitial atoms and vacancy sharply increase. Vacancies combine with each other and make the formation of voids and He bubbles, which is harmful to mechanical properties. Thus, one of effective method to decrease irradiation-induced damage is to provide amount of sites for voids to annihilate. The main structural differences between NbMoTaW and NbMoTaWRe RHEAs are the grain sizes, i.e. the number of grain boundaries, and grain boundary features. Excess volumes in NbMoTaWRe RHEA lead to formation of amorphous regions in grain boundaries, as shown in Fig. 4(b). Irradiation induced damages, such as voids, interact with grain boundaries, which causes He bubbles aggregate to the grain boundaries in NbMoTaW, as shown in Fig. 6(a). In NbMoTaWRe RHEAs, amorphous regions in grain boundaries provide a lot of sites to accelerate the annihilation of irradiated damage. Thus, the He bubble is much smaller in NbMoTaWRe RHEA than in NbMoTaW RHEA. What is more, He bubble segregation in grain boundary lead to severe brittlement in

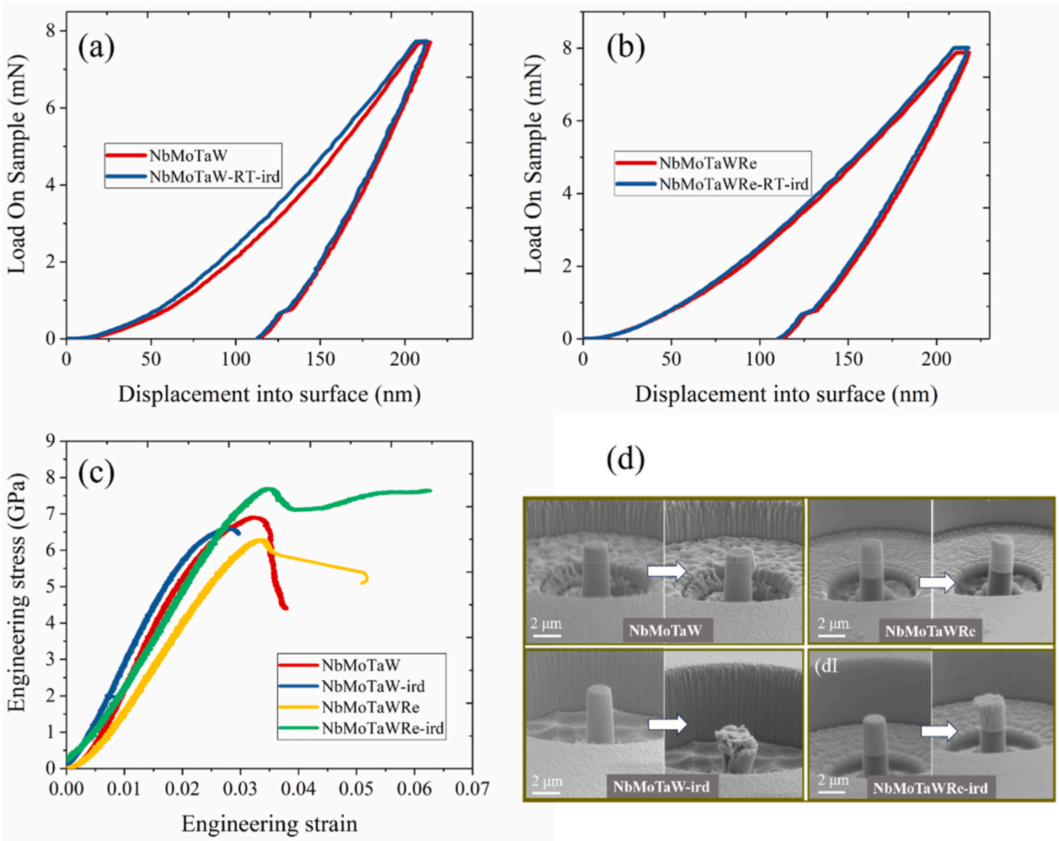

Fig. 5. Mechanical properties of NbMoTaW and NbMoTaWRe RHEAs before and after irradiation. Load - displacement curves of NbMoTaW RHEA are shown in (a), of NbMoTaWRe RHEA are shown in (b). Pillar compression results are shown in (c).

irradiated NbMoTaW.

4. Conclusions

The influences of Re on the mechanical and irradiated responses of NbMoTaW RHEA are investigated in this work via nano-indentation tests and micro-pillar compressions. Our researches justify the benefits of Re to irradiated properties in refractory alloys, such as Nb, Mo, Ta and W. The addition of Re enhances lattice distortion and excess volumes in NbMoTaW RHEA, which facilitates the annihilation of irradiated damage. Thus, irradiation-induced hardening embrittlement are less severe in NbMoTaWRe RHEA than in NbMoTaW RHEA, because He bubbles segregate to grain boundaries in NbMoTaW RHEA, while distribute relatively uniformly in NbMoTaWRe RHEA. In summary, the addition of Re not only refines grains, but also increases the excess volumes in NbMoTaW RHEA, which effectively enhances irradiation-resistance.

CRediT authorship contribution statement

Li Huang: Writing – review & editing, Writing – original draft, Conceptualization. **Shuo Sun:** Data curation. **Jianrong Xue:** Formal analysis. **Xiaohui Lin:** Investigation. **Xuanqiao Gao:** Supervision. **Yanchao Li:** Validation. **Jianfeng Li:** Funding acquisition. **Chunfang Ma:** Writing – review & editing. **Wen Zhang:** Supervision.

Data availability statement

The data that support this study are available from the corresponding author upon reasonable request.

Declaration of competing interest

The authors declare that they have no known competing financial interests or personal relationships that could have appeared to influence the work reported in this paper.

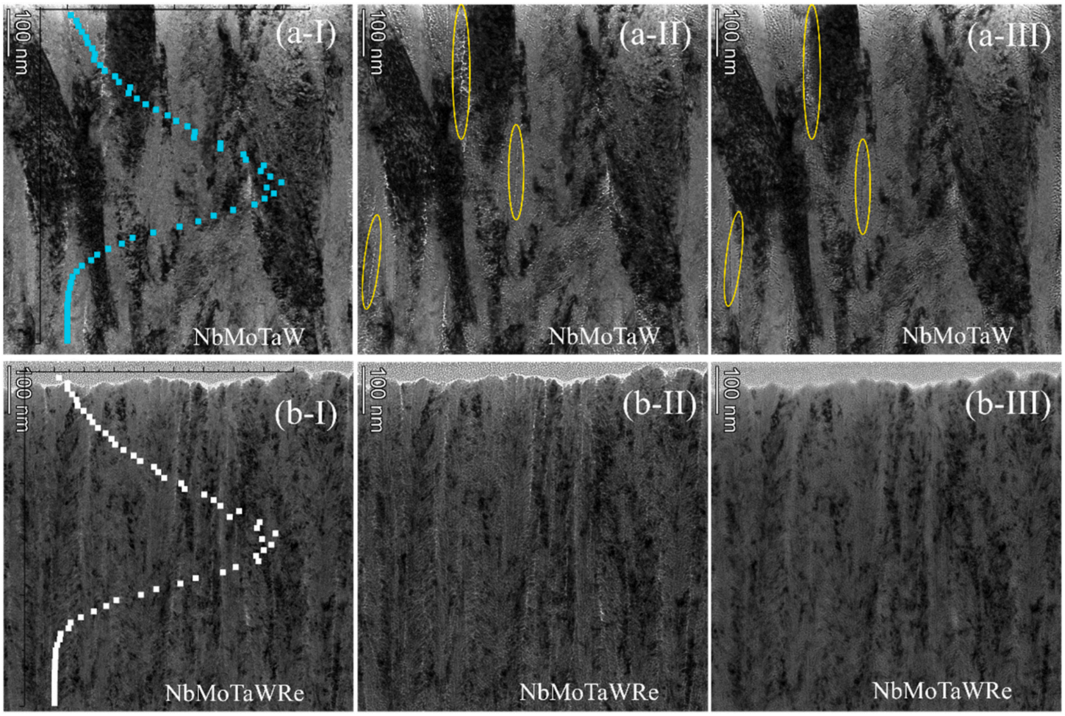

Fig. 6. TEM results for NbMoTaW in (a) and NbMoTaWRe RHEAs in (b) after irradiation. (a-II) and (b-II) are pictures with focus - 500 nm, and (a-III) and (b-III) are pictures with focus + 500 nm. Inserts in (a-I) and (b-I) are the distributions of He concentration that based on SRIM calculation.

Acknowledgements

This research is funded by Xi'an Association for Science and Technology, No. 095920221329, and by Qin Chuang Yuan Project of Department of Science and Technology of Shaanxi Province, No. QCYRCXM-2022-164, and by Northwest Institute for Nonferrous Metal Research, No. YK2301, and by Natural Science Funding of Shaanxi Province, No. 2024GX-YBXM-365, and by Natural Science Basis Research Plan in Shaanxi Province of China, No. 2022JQ-421.

References

[1] V. Zin, F. Montagner, E. Miorin, et al., Effect of Mo content on the microstructure and mechanical properties of CoCrFeNiMox HEA coatings deposited by high power impulse magnetron sputtering, Surf. Coating. Technol. 476 (2024) 130244, https://doi.org/10.1016/j.surfcoat.2023.130244.
[2] K. Zheng, J.Q. Tang, W.J. Jia, et al., Microstructure and mechanical properties of Al0.5CoCrFeNi HEA prepared via gas atomization and followed by hot-pressing sintering, J. Mater. Res. Technol. 30 (2024) 5323–5333, https://doi.org/10.1016/j.jmrt.2024.04.231.
[3] Y.T. Wu, C.C. Du, Z.L. Yu, et al., Effect of Cu content on the microstructure and mechanical properties of Fe20Co30Ni10Cr20Mn20 FCC-typed HEAs, Mater. Sci. Eng., A 897 (2024) 146336, https://doi.org/10.1016/j.msea.2024.146336.
[4] A.K. Ipadeola, A.K. Lebechi, L. Gaolatlhe, et al., Porous high-entropy alloys as efficient electrocatalysts for water-splitting reactions, Electr. Commun. 136 (2022) 107207, https://doi.org/10.1016/j.elecom.2022.107207.
[5] A.K. Lebechi, A.K. Ipadeola, K. Eid, et al., Porous spinel-type transition metal oxide nanostructures as emergent electrocatalysts for oxygen reduction reactions, Nanoscale 14 (2022) 10717–10737, https://doi.org/10.1039/D2NR02330J.
[6] B. Salah, A.K. Ipadeola, A.M. Abdullah, et al., Unravelling the alloy effect of porous binary Pd-based nanostructures on electrocatalytic oxidation of carbon monoxide in different electrolytes, ACS Appl. Eng. Materi. 1 (2023) 2196–2206. https://pubs.acs.org/doi/10.1021/acsaenm.3c00281.
[7] J.E.M. Torrento, T.S. P Sousa, N.C. Cruz, et al., Aging temperature effect on the phase composition, microstructure, and selected mechanical properties of non-equiatomic TiZrNbTaMo/Mn HEAs targeted for biomedical implants, Mater. Char. 208 (2024) 113678, https://doi.org/10.1016/j.matchar.2024.113678.
[8] G.B. Wilks Senkov, D.B. Miracle, et al., Refractory high-entropy alloys, Intermetallics 18 (2010) 1758, https://doi.org/10.1016/j.intermet.2010.05.014.
[9] G.B. Wilks Senkov, J.M. Scott, etal. Mechanical properties of $Nb_{25}Mo_{25}Ta_{25}W_{25}$ and $V_{20}Nb_{20}Mo_{20}Ta_{20}W_{20}$ refractory high entropy alloys, Intermetallics 19 (2011) 698, https://doi.org/10.1016/j.intermet.2011.01.004.
[10] Y.X. Xiong, K. Wang, S.J. Zhao, Surface damage of refractory high entropy alloys subject to He irradiation, J. Nucl. Mater. 595 (2024) 155060, https://doi.org/10.1016/j.jnucmat.2024.155060.
[11] J.R. Zhou, M. Kirk, P. Baldo, et al., Phase stability of novel HfNbTaTiVZr refractory high entropy alloy under ion irradiation, Mater. Lett. 305 (2021) 130789, https://doi.org/10.1016/j.matlet.2021.130789.
[12] J. Li, G. Pu, H.X. Sun, et al., Effect of He-ions irradiation on the microstructure and mechanical properties of TiTaNbZr refractory medium-entropy alloy film, Vacuum 217 (2023) 112545, https://doi.org/10.1016/j.vacuum.2023.112545.
[13] A.A. Rotkovich, D.I. Tishkevich, I.U. Razanau, et al., Development and study of lightweight recycled composite materials based on linear low-density polyethylene and W for radiation application, J. Mater. Res. Technol. 30 (2024) 1310–1318, https://doi.org/10.1016/j.jmrt.2024.03.187.
[14] A.V. Trukhanov, A.L. Kozlovskiy, A.E. Ryskulov, et al., Control of structural parameters and thermal conductivity of BeO ceramics using heavy ion irradiation and post-radiation annealing, Ceram. Int. 45 (12) (2019) 15412–15416, https://doi.org/10.1016/j.ceramint.2019.05.039.
[15] D.I. Tishkevich, A.A. Rotkovich, S.A. German, et al., Heavy alloy based on tungsten and bismuth: fabrication, crystal structure, morphology, and shielding efficiency against gamma-radiation, RSC Adv. 13 (2013) 24491–24498, https://doi.org/10.1039/D3RA04509A.

[16] A.K. Ipadeol, A.K. Lebechi, Le Gaolatlhe, et al., Porous high-entropy alloys as efficient electrocatalysts for water-splitting reactions, Electr. Commun. 136 (2022) 107207, https://doi.org/10.1016/j.elecom.2022.107207.
[17] Belal Salah, A.K. Ipadeola, A.M. Abdullah, et al., Unravelling the alloy effect of porous binary Pd-based nanostructures on electrocatalytic oxidation of carbon monoxide in different electrolytes, ACS Appl. Eng. Mater. 1 (8) (2023) 2196–2206. https://pubs.acs.org/doi/10.1021/acsaenm.3c00281.
[18] G. Pu, K. Zhang, L. Yang, et al., Irradiation-enhanced superficial modification and evolution of mechanical behavior in TaTiNbZr refractory high entropy alloy films exposed to low energy He plasma, J. Nucl. Mater. 577 (2023) 154337, https://doi.org/10.1016/j.jnucmat.2023.154337.
[19] S. Chang, K. Kai Tseng, T.Y. Yang, et al., Irradiation-induced swelling and hardening in HfNbTaTiZr refractory high-entropy alloy, Mater. Lett. 272 (2020) 127832, https://doi.org/10.1016/j.matlet.2020.127832.
[20] D. Li, N. Jia, H. Huang, et al., He ion irradiation enhanced precipitation and the impact on cavity formation in a HfNbZrTi refractory high entropy alloy, J. Nucl. Mater. 552 (2021) 153023, https://doi.org/10.1016/j.jnucmat.2021.153023.
[21] H.Z. Zhang, Z.B. Zhu, H.F. Huang, et al., Microstructures, mechanical properties, and irradiation tolerance of the Ti–Zr–Nb–V–Mo refractory high-entropy alloys, Intermetallics 157 (2023) 107873, https://doi.org/10.1016/j.intermet.2023.107873.
[22] Ö. Güler, D. Yılmaz, M. Sait Kanca, et al., Radiation shielding properties of composites of TiZrNbHfTa refractory high entropy alloy reinforced with TiZrNbHfTaOx high-entropy oxide, J. Alloy. Compod. 995 (2024) 174815, https://doi.org/10.1016/j.jallcom.2024.174815.
[23] X.L. Ren, W.W. Zhang, B.D. Yao, et al., The prediction of untraceable solute behaviors of helium in high-entropy alloys, J. Nucl. Mater. 547 (2021) 152820, https://doi.org/10.1016/j.jnucmat.2021.152820.
[24] S.R. Agnew, T. Leonhardt, The low-temperature mechanical behavior of molybdenum-rhenium, JOM 55 (10) (2003) 25–29, https://doi.org/10.1007/s11837-003-0171-2.
[25] A.V. Krajnikov, F. Morito, M.I. Danylenko, Embrittlement of molybdenum–rhenium welds under low and high temperature neutron irradiation, J. Nucl. Mater. 444 (2014) 404–415, https://doi.org/10.1016/j.jnucmat.2013.10.027.
[26] D.L. Yan, K.K. Song, H.G. Sun, et al., Microstructures, mechanical properties, and corrosion behaviors of refractory high-entropy ReTaWNbMo alloys, J. Mater. Eng. Perform. 29 (2020) 399–409, https://doi.org/10.1007/s11665-019-04540-y.
[27] J. Zhang, Y.Y. Hu, Q.Q. Wei, et al., Microstructure and mechanical properties of $Re_xNbMoTaW$ high-entropy alloys prepared by arc melting using metal powders, J. Alloy. Compods 827 (2020) 154301, https://doi.org/10.1016/j.jallcom.2020.154301.
[28] B. Zhang, Y. Mu, M.C. Gao, et al., On single-phase status and segregation of an as-solidified septenary refractory high entropy alloy, MRS Commun. 7 (2017) 78, https://doi.org/10.1557/mrc.2017.7.
[29] Y.P. Li, G. Ran, Y.J. Guo, et al., The evolution of dislocation loop and its interaction with pre-existing dislocation in He^+-irradiated molybdenum: *in-situ* TEM observation and molecular dynamics simulation, Acta Mater. 201 (2020) 462–476, https://doi.org/10.1016/j.actamat.2020.10.022.
[30] J. Fu, Y. C Chen, J.Z. Fang, et al., Molecular dynamics simulations of high-energy radiation damage in W and W-Re alloysm, J. Nuc, Mater 524 (2019) 9–20, https://doi.org/10.1016/j.jnucmat.2019.06.027.
[31] X. Qiu, H. Pang, G. Ran, et al., In-situ TEM observation of loop evolution in Mo-5Re alloy under Fe^+ irradiation, J. Nucl. Mater. 559 (2022) 153443, https://doi.org/10.1016/j.jnucmat.2021.153443.
[32] Eiji Kusano, Revisitation of the structure zone model based on the investigation of the structure and properties of Ti, Zr, and Hf thin films deposited at 70–600 °C using DC magnetron sputtering, J. Vac. Sci. Technol. A 36 (2018) 041506, https://doi.org/10.1116/1.5036555.
[33] Yuting Guo, Peng Zhang, Xiaonan Zhang, et al., Study on the microstructural evolution in NbMoTaW series refractory multi-principal element alloy films by low-energy and high-flux He ions irradiation, Surf. Coating. Technol. 452 (2023) 129140, https://doi.org/10.1016/j.surfcoat.2022.129140.